Electrochimica Acta 340 (2020) 135954

Contents lists available at ScienceDirect

Electrochimica Acta

journal homepage: www.elsevier.com/locate/electacta

Synthesis of highly efficient $Cu_2ZnSnS_xSe_{4-x}$ (CZTSSe) nanosheet electrocatalyst for dye-sensitized solar cells

Mahyar Mohammadnezhad [a], Mimi Liu [b], Gurpreet Singh Selopal [a, c, **], Fabiola Navarro-Pardo [a, c], Zhming M. Wang [c], Barry Stansfield [a], Haiguang Zhao [d], Cheng-Yu Lai [b], Daniela R. Radu [b, e, ***], Federico Rosei [a, *]

[a] Institut National de la Recherche Scientifique, Centre Énergie, Matériaux et Télécommunications, 1650 Boul. Lionel Boulet, Varennes, Québec, J3X 1S2, Canada
[b] Department of Mechanical and Materials Engineering, Florida International University Miami, FL 33174, USA
[c] Institute of Fundamental and Frontier Sciences, University of Electronic Science and Technology of China, Chengdu, 610054, PR China
[d] College of Physics & State Key Laboratory of Bio-Fibers and Eco-Textiles, Qingdao University, Qingdao, 266071, PR China
[e] Department of Materials Science and Engineering, University of Delaware, Newark, DE 19716, USA

ARTICLE INFO

Article history:
Received 19 October 2019
Received in revised form
11 February 2020
Accepted 23 February 2020
Available online 24 February 2020

Keywords:
Counter electrode
Dye-sensitized solar cells
CZTSSe nanosheets
Catalytic activity
Charge transfer resistance

ABSTRACT

$Cu_2ZnSnS_xSe_{4-x}$ (CZTSSe) has been reported as a promising platinum (Pt)-free counter electrode (CE) for dye-sensitized solar cells (DSSCs) with porous or crystalline structures. However, it is still challenging to develop a low-temperature method to synthesize CZTSSe electrodes with high surface area and excellent electrocatalytic activity. Herein, we present a low-temperature solution-phase synthetic approach to prepare self-organized CZTSSe nanosheets. As-synthesized CZTSSe nanosheets deposited on fluorine-doped tin oxide (FTO) substrate and applied as CE, yield a power conversion efficiency of (5.73%), which is comparable to the value we obtained using Pt-based CE (5.78%). In addition, CZTSSe nanosheets exhibit excellent electrocatalytic performance (4.60%) on carbon paper (CP) as a Pt/FTO-free CE. This impressive performance was attributed to the high specific surface area of CZTSSe with nanosheet morphology and related excellent electrocatalytic activity. Cyclic voltammetry and electrochemical impedance spectroscopy measurements confirmed that CE made of CZTSSe nanosheets have comparable catalytic activity with respect to Pt CE due to the low charge transfer resistance at the CE/electrolyte interface. The as-prepared CZTSSe CE with high reproducibility exhibits good chemical stability in the electrolyte containing. The low-temperature process, high surface area and high electrocatalytic activity help the CZTSSe nanosheets stand out as an alternative CE electrocatalyst in DSSC.

1. Introduction

Fossil fuels represent over 80% of the world's energy consumption. On the other hand, their decreasing availability, climate change and environmental pollution dictate an urgent transition towards renewable energy sources [1–3]. Amongst various carbon-free energy sources, solar technologies are particularly promising [1,2].

Since their invention in 1991, dye-sensitized solar cells (DSSCs) have been widely studied due to their promising features, such as cost-effective fabrication technology and eco-friendliness [4–6]. Considerable efforts have focused on using specially designed nanostructured materials to improve the performance and stability of the different components in DSSCs [7–11]. A typical DSSC consists of four main components: a wide bandgap semiconducting oxide, dye sensitizer molecules, an electrolyte, and a counter electrode (CE). During device operation, the CE plays an important role by collecting electrons from the external circuit and regenerating the oxidized iodide/triiodide redox couple electrolyte at the CE/electrolyte interface [12–14]. Thus, an ideal CE should possess the high electrocatalytic activity and exhibit excellent stability towards the electrolyte [6,15,16].

To date, CEs made of fluorine-doped tin oxide (FTO) glass coated

* Corresponding author.
** Corresponding author. I Institut National de la Recherche Scientifique, Centre Énergie, Matériaux et Télécommunications, 1650 Boul. Lionel Boulet, Varennes, Québec, J3X 1S2, Canada.
*** Corresponding author. Department of Mechanical and Materials Engineering, Florida International University Miami, FL 33174, USA.
E-mail addresses: gurpreet.selopal@emt.inrs.ca (G.S. Selopal), dradu@fiu.edu (D.R. Radu), rosei@emt.inrs.ca (F. Rosei).

https://doi.org/10.1016/j.electacta.2020.135954
0013-4686/

with a thin layer of platinum (Pt) are the most widely used as conventional CE material. However, as a noble metal, limited supply and high cost are unresolved challenges that need to be addressed for the large-scale commercialization of DSSCs [17]. Pt/FTO CEs used in DSSCs accounts for more than 40% of the total device cost [18–20]. In addition, Pt/FTO CE is not stable in contact with some electrolytes such as cobalt complexes and polysulfide electrolytes [21]. To overcome these issues and deploy commercial DSSCs, the design/fabrication of Pt-free CEs, without reducing its electrocatalytic activity and stability is a key factor. In this regard, major efforts have focused on replacing Pt with abundant low-cost narrow bandgap p-type semiconductors [10,22–25].

Copper chalcogenide-based compounds as p-type semiconductors are considered promising materials for use as CEs in DSSCs [17,23,26–28]. Among these, Earth-abundant copper-zinc-tin-chalcogenide $Cu_2ZnSnS_xSe_{4-x}$ (CZTSSe) is an interesting material due to its electronic structure, bandgap, and synergetic effects of the different elements [17,21,29]. Xin et al. [17] first introduced CZTSSe film as a potential substitute for Pt in low-cost CEs for the triiodide/iodide electrolyte reduction. They employed a simple solution-phase chemical synthesis approach to prepare the Cu_2ZnSnS_4 (CZTS) nanocrystal dispersion that can be coated on the FTO substrate. The CZTS thin film is then sintered at 540 °C for 1 h in selenium (Se) vapor for selenization and yields CZTSSe. Chen et al. [21] reported the effect of the crystallization of CZTSSe film on DSSCs performance. The CZTSSe film was produced by evaporation of 40 mg of Se powder mixed with Ar in a graphite box at 550 °C for 30 min. It was found that the formation of a high-crystallinity film with large grains dramatically improved the charge transport process. Shen et al. [27] explored a screen-printing process for CZTSSe CEs. Similar to previous work, CZTSSe film was prepared by screen-printing CZTS pastes (followed by heating at 400 °C for 15 min in the air to remove the organic binders), then by post selenization (at 500 °C for 10 min) using Se vapor obtained from elemental Se pellets. Although previous work [17,21,27] demonstrated a very exciting approach for the application of CZTSSe as a CE in a DSSC, there are two crucial factors that must be considered: (i) synthesis of CZTSSe by post selenization requires high temperatures (higher than 500 °C) and special annealing environment; (ii) previous studies mainly focused on designing crystalline films that could limit the surface contact between CE and electrolyte. The major issue in these reports is the post selenization reaction of the deposited film at high temperatures that could create cracks in the film due to the significant thermal stress.

Herein we report the synthesis of CZTSSe nanosheets as efficient CEs for DSSCs. The aim of this work was to use as-synthesized CZTSSe with intrinsic Se content to remove the high-temperature selenization process and related negative impact (thermal stress). In addition, we synthesized the CZTSSe with nanosheets morphology to increase the active catalytic surface area of the CE.

The as-prepared CZTSSe nanosheets could be effectively dispersed in ethanol and the resulting ink was used to fabricate the CZTSSe thin films on FTO substrates as Pt-free CEs in DSSCs. The CZTSSe nanosheets CE exhibit excellent electrocatalytic activity and stability for triiodide/iodide electrolyte reduction with high reproducibility and a comparable PCE (5.73%) to that based on conventional Pt CEs (5.78%). On the other hand, when CZTSSe nanosheets deposited on the carbon paper (CP) as a FTO and Pt free CE, exhibits a comparable PCE (4.60%).

2. Materials and methods

2.1. Materials

All chemical reagents and solvents in this work were used as received, without further purification. Tin(IV) bis(acetylacetonate) dichloride ($SnCl_2(C_5H_7O_2)_2$, 98%), copper(II) chloride dihydrate ($CuCl_2 \cdot 2H_2O$, 99.999%), zinc diethyldithiocarbamate ($[(C_2H_5)_2NCS_2]_2Zn$, 97%), selenium (Se) (99%), oleylamine (OLA, 70%), 1-Dodecanethiol (1-DDT, ≥ 98%), and 1-Butanethiol ($CH_3(CH_2)_3SH$, 99%) were purchased from Sigma-Aldrich. ACS grade chloroform (99.8%), toluene (99.7%), acetone (99.8%), methanol (99.8%) and ethanol (99.5%) were purchased from VWR International. Glass substrates were bought from Fisher Scientific.

2.2. Preparation of $SnSe_2$ nanosheets

In a typical experiment, $SnCl_2(C_5H_7O_2)_2$ (1 mmol, 387.8 mg) and 20 mL of oleylamine (OLA) were loaded into a 100 mL two-necked round-bottom quartz flask at room temperature and degassed for 30 min by stirring the mixture under vacuum. In parallel, the Se powder (2 mmol, 157.9 mg) together with 2 mL of OLA and 2 mL of 1-DDT were added to a two-necked 25 mL round-bottom flask, followed by stirring under vacuum at room temperature for 30 min. Next, the Sn (II) solution was heated to 140 °C under an argon atmosphere, while keeping the Se solution at room temperature (under argon atmosphere). Once the temperature of the Sn solution reached 140 °C, the Se solution was injected in the Sn (II) solution flask. Further, the reaction was heated to 220 °C and kept at this temperature for 1 h. The reaction was quenched by removing the heating source and cooling to room temperature. The solids were decanted and washed with a mixture of OLA (8 mL) and 1-DDT (1 mL) to remove residual Se. Subsequently, the $SnSe_2$ nanosheets were collected by centrifugation and purified by washing three times with a mixture of chloroform and ethanol (V: V, 1: 3). The final product was dried overnight in a vacuum oven at 45 °C.

2.3. Preparation of CTSe nanosheets

The formed $SnSe_2$ nanosheets were used as starting material for the fabrication of CTSe, by copper incorporation in the $SnSe_2$ lattice. The Cu precursor was prepared by mixing $CuCl_2 \cdot 2H_2O$ (1.6 mmol, 272 mg) and 4 mL of OLA in a 25-mL two-necked round bottom flask and stirring the mixture under vacuum at 100 °C for 30 min. Upon backfilling the flask with argon, the Cu (II) solution was injected into the $SnSe_2$ suspension. The reaction was raised to 220 °C and kept at that temperature for 1 h. The reaction was quenched by removing the heat and natural cooling to room temperature. Using the same purification process as for the $SnSe_2$ nanosheets, the CTSe precipitate was decanted, washed with a mixture of OLA (8 mL) and 1-DDT (1 mL), and then collected by centrifugation. The nanosheets were further purified by washing three times with a mixture of chloroform and ethanol (V:V, 1:3). The collected product was dried overnight in a vacuum oven at 45 °C.

2.4. Preparation of CZTSSe nanosheets

CTSe was used as an originating lattice to fabricate CZTSSe. In a typical experiment CTSe (0.5 mmol, 241 mg), along with $Zn(S_2NEt_2)_2$ (0.5 mmol, 181 mg) and 20 mL of OLA were loaded in a two-neck 100 mL round-bottom quartz flask and the entire mixture was stirred under vacuum for 30 min at room temperature. The reaction was further heated to 300 °C and held at the same temperature for 1 h. After the reaction, the mixture was quenched by removing the heating source and allows cooling naturally. The precipitate was collected by centrifugation and purified by washing three times with a mixture of chloroform and ethanol (V: V, 1:3). The resulting CZTSSe product was dried overnight in a vacuum oven at 45 °C.

2.5. CE fabrication

FTO coated glasses were ultrasonically cleaned with water and soap, acetone and isopropanol for 20 min then dried with nitrogen gas. The coating dispersion (ink) was prepared by dissolving 2 mg of CZTSSe in 1 mL ethanol and sonicating in a water bath for 120 min. The cleaned FTO substrates were spin-coated with CZTSSe ink over different cycles (rotation speed of 3000 rpm with an acceleration of 1000 rpm for 30 s), followed by annealing at 100 °C for 10 min under ambient air conditions to ensure complete solvent removal. The CZTSSe nanosheets were deposited into CP by electrophoretic deposition (EPD) under direct current (DC) bias of 150 V for 120 min. The Pt coated FTO/glass substrate CEs with 10 nm thickness were prepared using a RF magnetron sputtering system (Kurt J. Lesker, CM818).

2.6. Device fabrication

The TiO_2 blocking layer was coated on the FTO substrates using a single step spin-coating (rotation speed of 6000 rpm with an acceleration of 2000 rpm for 30 s), followed by annealing at 500 °C for 30 min under ambient air conditions. The TiO_2 mesoporous film was then deposited on top of the blocking layer using the tape casting method. Mesoporous TiO_2 photoanodes are composed of two layers: (i) an active layer of 20 nm-sized anatase TiO_2 nanoparticles (18 NR-T from Dyesol) and (ii) a scattering layer of 150–250 nm sized particles (WER2-O from Dyesol). The FESEM images of the as-prepared TiO_2 mesoporous film on the FTO glass substrate are shown in Fig. S1. Subsequently, the samples were annealed at 500 °C for 30 min under ambient air conditions. The XRD analysis of the annealed TiO_2 mesoporous film is shown in Fig. S2 that confirmed the anatase phase of TiO_2. For dye-loading, the prepared photoanodes were immersed into a 0.5 mM ethanolic solution of commercial Ru-based molecular complex N719 dye for 24 h. The DSSC devices were sealed with a 60 μm thick thermal-plastic spacer (Meltonix 1170-60 PF, Solaronix), and an iodide/triiodide electrolyte injection was performed.

2.7. Characterization

X-ray diffraction (XRD) patterns of the synthesized powders and films were collected with a Rigaku-MiniFlex600 (Cu K_α radiation, $\lambda = 1.5405$ Å). Raman spectroscopy was performed with a Horiba Scientific spectrometer equipped with an Ar laser source ($\lambda = 532$ nm). The morphology of the prepared materials and films was characterized by scanning electron microscopy (FE-SEM, JEOL JSM-6900 F) equipped with an energy-dispersive X-ray spectrometer (EDS), and transmission electron microscopy (ZeissLibra120-TEM). ImageJ software was used to analysis electron microscopy images. A UV-Vis-NIR spectrophotometer (UV-3600 plus-SHIMADZU) equipped with an integrating sphere was employed to measure the absorption spectra of the nanosheet thin films. Thermogravimetric analysis (TGA) (HITACHI-STA7200) was used to determine the nanosheets thermal stability. Cyclic voltammetry (CV) was carried out in a Solartron SI 1287 potentiostat galvanostat using a three-electrode system, at a scan rate of 10 mVs^{-1}. As-fabricated CEs (CZTSSe and Pt) acted as the working electrode, Ag/AgCl as a reference electrode and Pt plate as a counter electrode in diluted iodide/triiodide electrolyte in acetonitrile (20 times). Electrochemical impedance spectroscopy (EIS) was carried out under dark conditions using a SOLARTRON 1260 A. EIS results were analyzed using an appropriate equivalent circuit model with Z-View software. The chemical composition of the synthesized CZTSSe nanosheets was determined by X-ray photoelectron spectroscopy (XPS) in a VG Escalab 220i-XL equipped with an Al K_α source. The photocurrent-voltage (J-V) measurements were produced by a Keithley 2400 Source Meter under simulated sunlight with an ABET2000 solar simulator at AM 1.5G (100 mW cm^{-2}).

3. Results and discussion

3.1. Characterization of the as-prepared CZTSSe nanosheets

Fig. 1(a) shows the XRD patterns of the as-synthesized CZTSSe nanosheets. The diffraction pattern displays three main characteristic peaks at $2\theta = 27.39°$, 45.53° and 53.92° which can be attributed to the (112), (220/204) and (312/116) planes of CZTSSe, respectively. According to the standard XRD pattern of CZTSe (JCPDS Card, No. 01-070-8930), these peaks moved to higher angles due to the expansion of the unit cell upon replacement of small S (1.84 Å) with large Se atoms (1.98 Å) [27,30]. We developed a cascade approach to the solution-phase preparation of ultra-thin CZTSSe nanosheets, starting with 2D $SnSe_2$ as an originating lattice to synthesize ultra-thin CTSe nanosheets, subsequently used in the same fashion to generate 2D CZTSSe. The XRD peaks of the CZTSSe are slightly broadened and asymmetric due to some impurity phase in the final product. This implies the presence of CZTS in final CZTSSe nanosheets that is in good agreement with the Raman spectrum acquired from the as-prepared CZTSSe nanosheets. Figs. S3–S4 show the XRD patterns acquired from $SnSe_2$ and CTSe, which confirm their excellent crystallinity. The Raman spectrum of the as-prepared CZTSSe nanosheets is shown in Fig. 1(b). The A_1 Raman mode frequencies of CZTSe and CZTS are detected at 189.3 cm^{-1} and 323.9 cm^{-1}, respectively which are in good agreement with the literature indicating the formation of pure CZTSSe [21,30,31]. The Raman spectrum of the synthesized $SnSe_2$ nanosheets (Fig. S5) shows the Raman active modes E_g (113.6 cm^{-1}) and A_{1g} (182.6 cm^{-1}), respectively, confirming the presence of the reported 2-H polytype $SnSe_2$ [32]. The Raman spectrum of the CTSe obtained from the $SnSe_2$ nanosheets (Fig. S6) shows three peaks, uniquely identifying the CTSe with the Raman shifts at 175.8 cm^{-1} belonging to the A' mode of the CTSe crystal, and the two peaks at 201.6 cm^{-1} and 225.8 cm^{-1} corresponding to the A" mode of CTSe crystal [33]. The optical absorption properties of as-synthesized CZTSSe nanosheets were characterized by UV-Vis-NIR absorption spectrum of spin-coated thin films of dilute CZTSSe nanosheets dispersions on glass substrates, see Fig. 1(c). The direct optical band gap was estimated from Tauc plots. The absorption spectrum reveals a broad absorption in the visible region. The bandgap of the synthesized CZTSSe nanosheets estimated from the Tauc plot (SI) is ~1.42 eV, consistent with previous reports [30,34]. The stability of the synthesized $SnSe_2$, CTSe and CZTSSe nanosheets was determined by thermogravimetric analysis (TGA). TGA plots show decomposition of CZTSSe nanosheets starts at temperatures above 700 °C that confirm high stability of CZTSSe under thermal stress, see Fig. 1(d) and S7-S8.

The detailed structure and morphology of as-prepared CZTSSe nanosheets were investigated by FESEM and TEM. The FESEM image shows the formation of the hierarchical microsphere morphology with an average diameter of ~2.5 μm that is composed of a group of nanosheets, see Fig. 2(a). Figs. 2(b) and S9 shows the high magnification FESEM image of CZTSSe nanosheets with an average thickness of ~20 nm. The root-mean-squared (RMS) roughness of the surface of nanosheets measured from FESEM images showed a rough surface with RMS roughness of 26.4 ± 4 nm. The structure of as-synthesized CZTSSe nanosheets is further characterized by elemental mapping using EDS. The results show that Cu, Zn, Sn, S and Se elements are homogeneously distributed in the selected region. Consistent with and XPS results, the EDS analysis also reveals that no obvious mixed impurity phases are

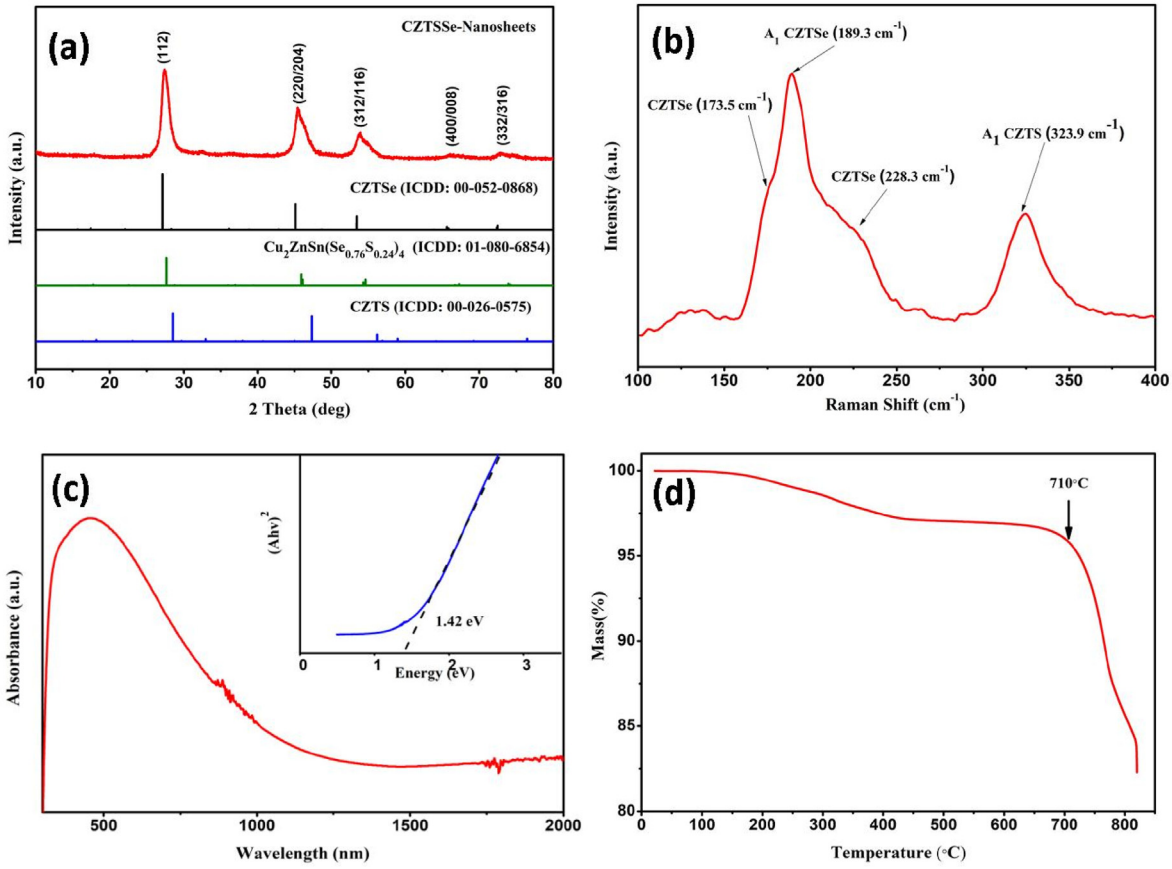

Fig. 1. (a) XRD pattern, (b) Raman spectra, (c) UV−Vis absorption spectra and (d) TGA plot of as-prepared CZTSSe.

observed. TEM imaging confirms the plate-shape of CZTSSe (Fig. 2(d) and (g)). SAED pattern shown the three concentric diffraction rings corresponding to the (112), (220) and (312) planes that match the structure of CZTSSe (Fig. 2(e)) and XRD results. The chemical composition of the nanosheets was characterized by EDS measurements. EDS spectrum is shown in Fig. 2 (h) confirm the presence of Cu, Zn, Sn, S, and Se in the CZTSSe system. HR-TEM is shown in Fig. 2 (f) that revealed the highly crystalline nature of CZTSSe nanosheets. The interplanar spacing of CZTSSe nanosheets was measured and found to be 3.18 Å, which is attributed to (112) crystallographic planes (Inset of Fig. 2 (f)). Figs. S10−S11 display the HR-TEM image of $SnSe_2$ and CTSe with layered morphology. The small size nanosheets are beneficial for coating fabrication since they easily disperse in the solvent to form a uniform ink [30]. The sheet structure can accelerate electron transport faster than the mu multigrain structure with large numbers of grain boundaries and defects [21,23]. Moreover, the nanosheets morphology could promote the formation of a large surface area for increasing the catalytic activity and accelerating charge transport, both being important factors for an ideal CE [21,30].

The elemental composition of the as-synthesized CZTSSe nanosheets was further examined with high-resolution XPS to confirm the presence of the five constituent elements in the sample. Fig. 3(b) shows the XPS spectrum of Cu 2p with two peaks located at 933.5 eV and 953.3 eV for Cu $2p_{3/2}$ and Cu $2p_{1/2}$, respectively. The peak positions and separation of 19.8 eV are in good agreement with that of Cu (I) [30,35,36]. The peaks of Zn 2p appear at binding energies of 1022.1 eV (Zn $2p_{3/2}$) and 1045.3 eV (Zn $2p_{1/2}$) with a peak separation of 23.2 eV imply the formation of Zn (II) [36,37]. The peak of Sn 3d is split into two peaks $3d_{5/2}$ and $3d_{3/2}$ with a split orbit of 8.7 eV, suggested the presence of Sn (IV) state [36,37]. Fig. 3(e) shows the binding energies S 2p with two peaks at 161.3 eV and 162.7 eV, indicating assigned to S valence state in CZTSSe compound S (II) [28,30,35]. There is another peak located at 166.3 eV, assigned to Se $3p_{1/2}$ [35]. The other peak at 55.3 eV is strong evidence for Se element in CZTSSe. The broad and low-intensity peak near 60.1 eV can be attributed to the surface oxidation state of selenium species [37,38].

3.2. Application of CZTSSe nanosheets as CE in DSSCs

To obtain high-efficiency DSSCs, a good quality film without defects and large contact area are necessary for electron transfer, catalytic reaction and fast regeneration of the oxidized electrolyte [10,14,23,39]. Fig. 4 shows SEM images acquired at different magnifications of CZTSSe thin films formed on the FTO substrate with different spin coating cycles. As observed in these images, the uniformity of the films is gradually enhanced by increasing the cycles of the spin coating. As displayed, the homogeneity of CZTSSe films before 5 cycles is very low, due to the non-uniform distribution of the nanosheets. However, a uniform CZTSSe film covers the FTO substrate after 5 cycles. CZTSSe nanosheets with uniform size distribution and good dispersibility are made up of many hierarchical microspheres, with each bunch consisting of several nanosheets. The combination of nanosheets together provided abundant pores, increasing the specific area of the catalytic material [23,34,39].

To investigate the influence of film morphology on the PV performance of the DSSCs, we measured the current-voltage characteristic of six different CEs. Fig. 5(a–e) and Table 1 display the

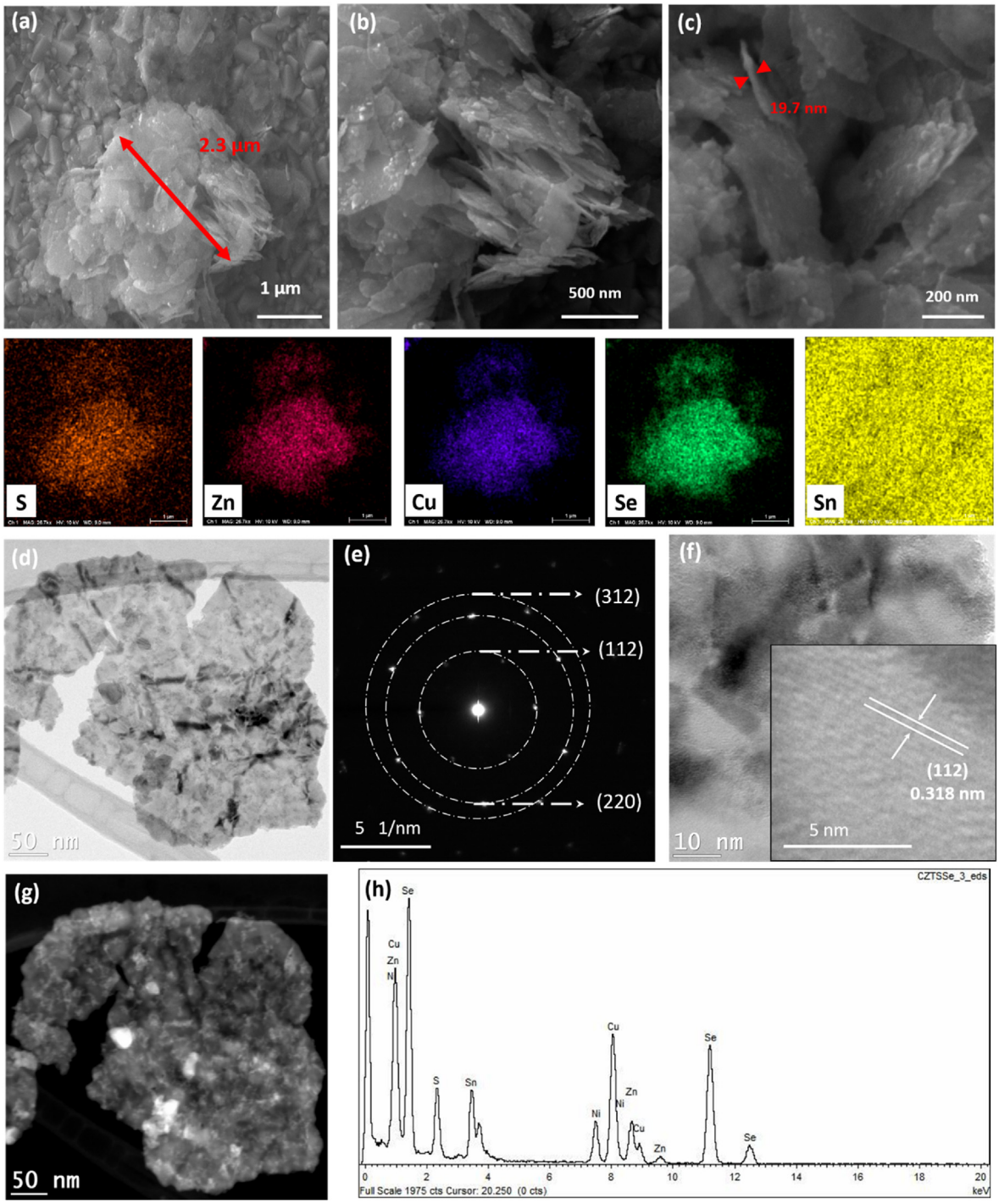

Fig. 2. Structural characterization of as-synthesized CZTSSe nanosheets: (a) FESEM images at low magnification and related EDS element mapping images. (b and c) High magnification. (d) Bright-field TEM image of one individual CZTSSe nanosheet, (e) SAED, (f) HR-TEM (g) dark-field TEM image, (h) EDS of the selected area.

photocurrent density-voltage (J-V) curves obtained under one sun simulated sunlight at AM 1.5G (100 mW cm^{-2}) and dark condition and corresponding photovoltaic parameters, such as the J_{sc}, V_{oc}, FF and PCE of DSSCs with CEs based on the CZTSSe and Pt. The results show that the structure of CZTSSe film has a significant influence on the PV parameters of DSSCs. As shown in Fig. 5 (a), the PCE of the device assembled with five cycles deposition is 17.77% higher than the one obtained with three cycles. The relatively high catalytic activity of CZTSSe CE fabricated with five or more cycles of coating deposition can be attributed to the uniformity and homogeneity of the CZTSSe film (Fig. 4). The significantly enhanced J_{sc} values contribute to the superior performance and indicate a rapid rate of hole recovery at the CZTSSe CEs and electrolyte interface [36,38]. The enhancement in J_{sc} and consequently PCE can be ascribed to the higher active surface area of the CEs compared to the samples that fabricated with 1 and 3 cycles. A high surface contact area of the CE/electrolyte and faster electrolyte reduction decrease the availability of tri-iodide ions to recombine with photo-injected

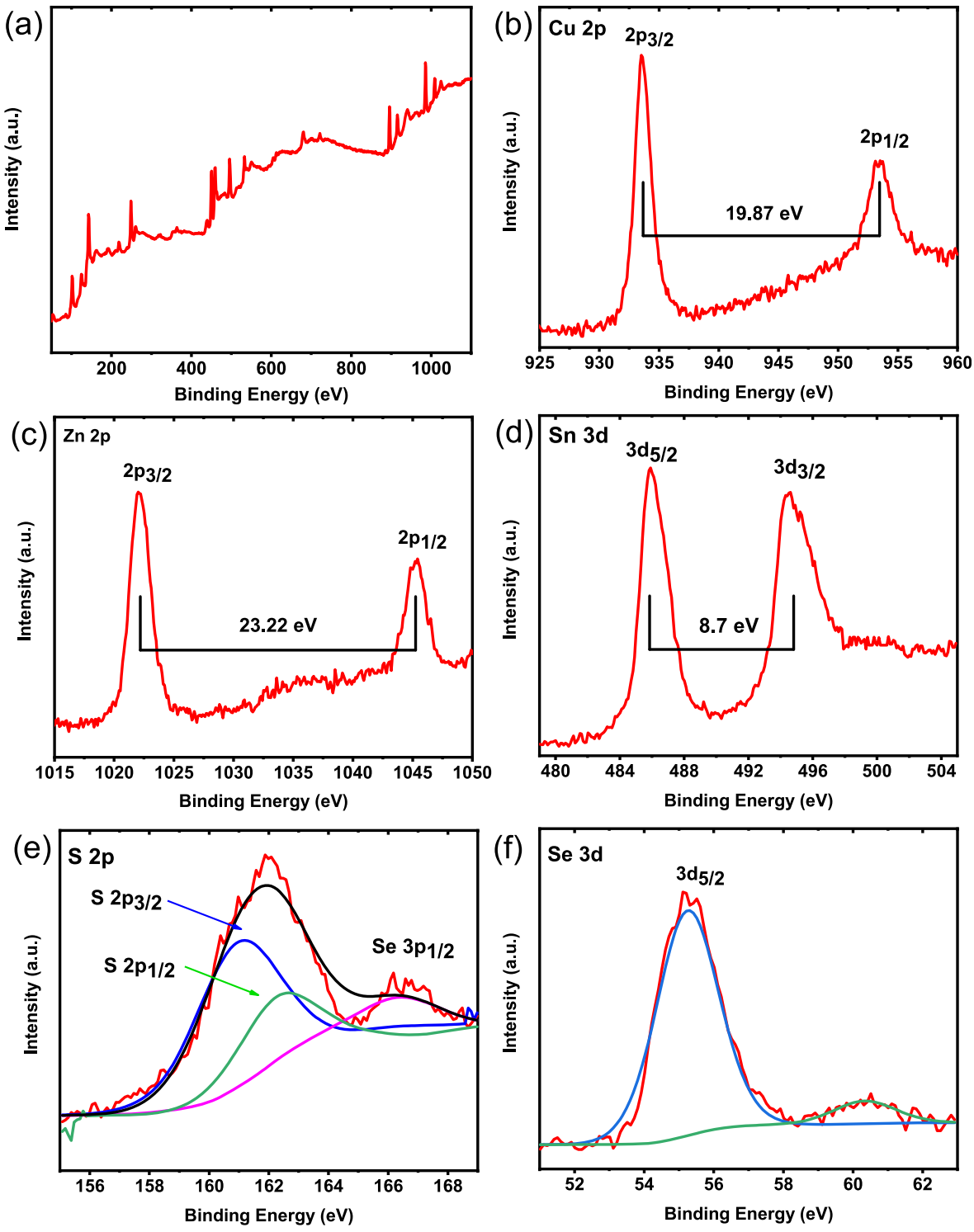

Fig. 3. XPS spectrum of the as-synthesized CZTSSe nanosheets (a) Cu 2p, (b) Zn 2p, (c) Sn 3d, (d) S 2p, (e) Se 3d.

electrons, thus resulting in improved performance [18,19,40]. Furthermore, the results show essentially the same value of V_{oc}. Based on the bandgap theory, the difference between the quasi-Fermi level of the semiconductor and the electrolyte determines the V_{oc} of the DSSC [6,23]. In a DSSC, the FF is mainly influenced by the series resistance of the CE, the resistance at the interface of CE/electrolyte, the transport resistance in photoanode, etc. The DSSC based on the CZTSSe CEs has a similar FF of with Pt CE due to the high charge transfer at the CE/electrolyte interface and catalytic ability [36,41]. The DSSC based on the CZTSSe CE (7 cycles), yielding a good power conversion efficiency (5.73%), which is comparable to that obtained using the Pt CE (5.78%).

In a DSSC, one of the main possible recombination reactions is the transfer of the injected electrons from the conduction band of the semiconductor to the oxidized state of the electrolyte. The considerable loss in performance of DSSCs can be ascribed to

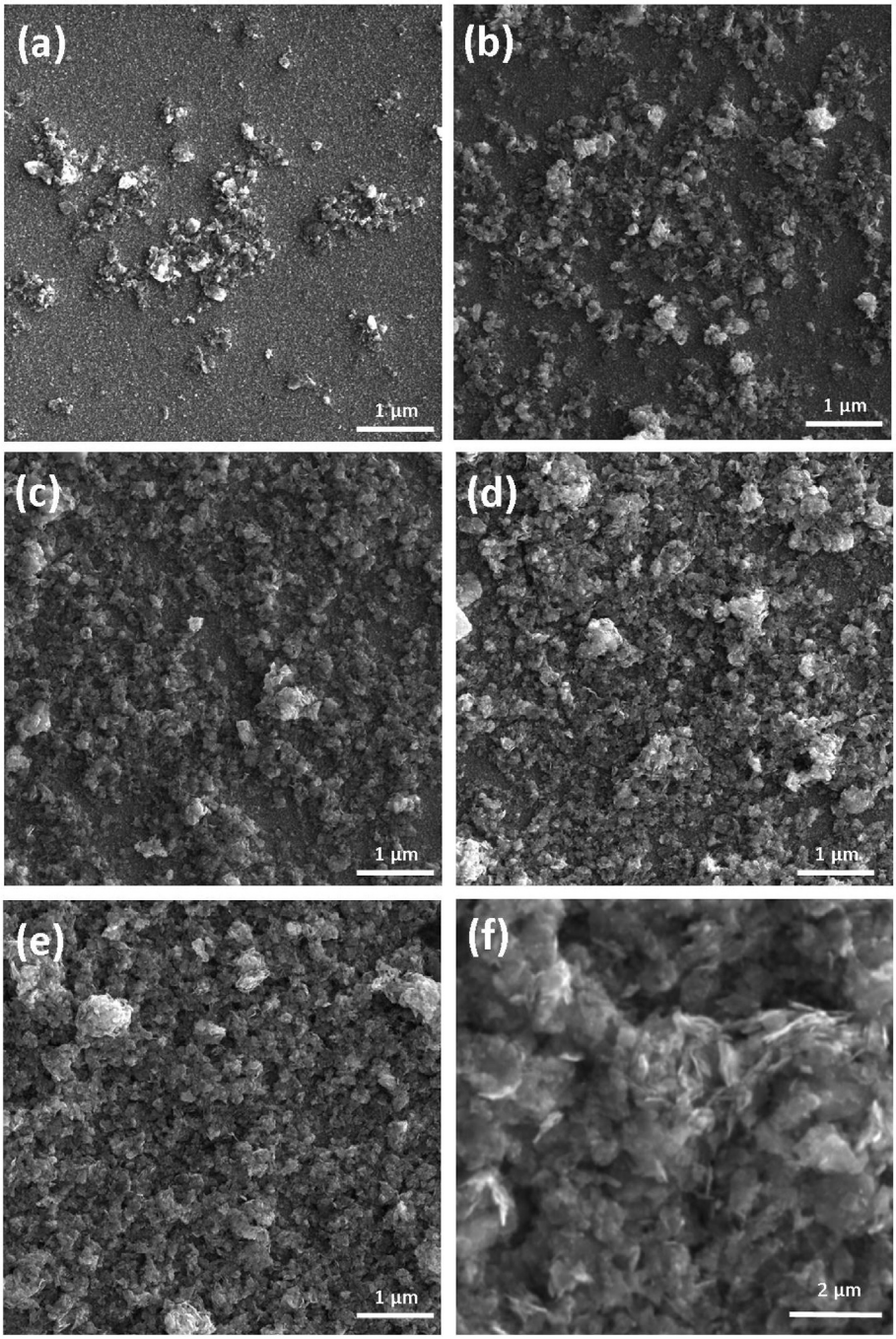

Fig. 4. FESEM images of CZTSSe film with different spin coating cycling on the FTO substrate: (a) 1 cycle, (b) 3 cycles, (c) 5 cycles, (d) 7 cycles, (e and f) 9 cycles.

various factors including undesirable carrier recombination at interfaces (TiO_2/dye/electrolyte and Pt/electrolyte), regeneration kinetics of oxidized dye molecules and redox couple electrolyte. The fast kinetics of the electrolyte reduction at the surface of the CE is a crucial factor for reducing recombination. Thus, the optimization of the CE structure to delay the interfacial charge recombination dynamics is a crucial factor to improve DSSC performance [39,42]. It has been shown that the limited recombination with the oxidized electrolyte results in a slower photovoltage decay [43]. The photovoltage decay and calculated electron lifetime (τ_e) [defined by using Equation (1)] curves of DSSCs assembled with different CEs are shown in Fig. 5 [44].

$$\tau_e = \left(-\frac{k_B T}{e}\right) \Big/ \left(\frac{dV_{oc}}{dt}\right) \quad (1)$$

In this equation T is the absolute temperature, k_B is Boltzmann's constant, and e is the elementary charge [44]. The results show that the photovoltage decay decreases when increasing the cycles of film deposition [Fig. 5 (f)]. The high τ_e of the DSSCs based on the CZTSSe CEs (7 cycles) is due to the uniform film and high surface area. The comparable photovoltage decay and lifetime of the CZTSSe and Pt CEs confirmed the strong ability of CZTSSe for electron collection and high electrocatalytic properties.

To gain more insight into the electrocatalytic ability of the

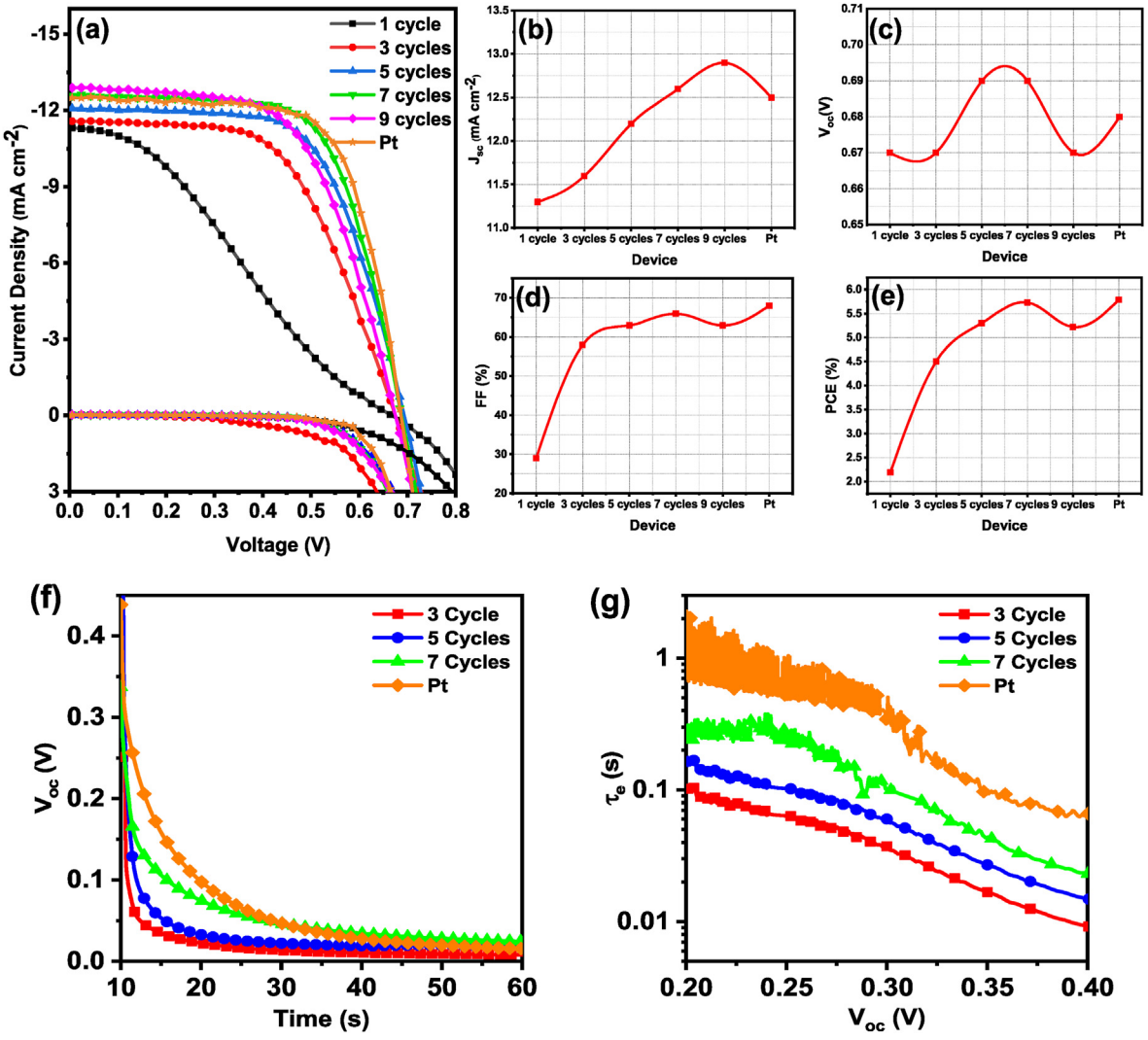

Fig. 5. Photovoltaic performances of the DSSCs assembled with different CEs (a) Current density-voltage curves of solar cells under AM1.5G irradiation (100 mW cm^{-2}) and dark, (b) J_{sc}, (c) V_{oc}, (d) FF and (e) PCE. Transient photovoltage decay measurement: (f) transient V_{oc} decay and (g) obtained electron lifetime (τ_e) for DSSCs assembled with different CEs.

Table 1
Performance parameters of DSSCs fabricated using different CEs.

Sample	PCE/%	FF/%	V_{oc}/V	J_{sc}/mA cm^{-2}
CZTSSe 1 cycle	2.19	29	0.67	11.3
CZTSSe 3 cycle	4.50	58	0.67	11.6
CZTSSe 5 cycle	5.30	63	0.69	12.2
CZTSSe 7 cycle	5.73	66	0.69	12.6
CZTSSe 9 cycle	5.22	63	0.67	12.9
Pt	5.78	68	0.68	12.5

prepared CEs, the electrochemical properties were evaluated using CV. The CV curves of CZTSSe and Pt electrodes are shown in Fig. 6 (a). All curves were obtained in the standard three-electrode system composed of a working electrode (CZTSSe and Pt), Pt plate as a counter electrode, Ag/AgCl as a reference electrode and iodide/triiodide electrolyte. Two typical pairs of oxidation-reduction peaks are observed in the CV curves, presenting superior electrocatalytic activity towards iodide/triiodide electrolyte. The peaks at more negative potentials correspond to the reduction of the electrolyte, whereas the right one at the high potential range is assigned to the oxidation [38,45]. The reduction and oxidation peak current densities of the sample produced with 7 cycles are higher than those deposited with 5 and 3 cycles, indicating that by increasing the spin coating cycling a higher amount of CZTSSe nanosheets is deposited on the substrate, as observed by FESEM. The current density of the reduction reaction of CZTSSe (seven cycles) is -0.022 mA cm^{-2}, that is more negative than that of the Pt-based electrode (- 0.015 mA cm^{-2}). The current density in the oxidation peak of the CZTSSe film deposited with seven cycles also is higher than those of the Pt, 0.11 and 0.09 mA cm^{-2}, respectively. These functional properties improvement should be attributed to the nanosheet architecture of the CZTSSe that can increase the active catalytic surface area of the CE. A higher specific surface area of the CE produces more catalytic sites, which is favorable for the electrolyte reduction. Thus, imparting a higher surface contact between electrolyte and catalysts is desirable for enhancing the catalytic activity of CEs [6,23]. These results indicate that CZTSSe nanosheets are as effective as Pt in catalyzing the reduction of the iodide/triiodide electrolyte.

Electrochemical impedance spectroscopy (EIS) measurements were further carried out to investigate the reaction kinetics at the CE/electrolyte interface. The EIS analysis was carried out in four symmetric cells fabricated with Pt and CZTSSe CEs. Fig. 6 (b) shows

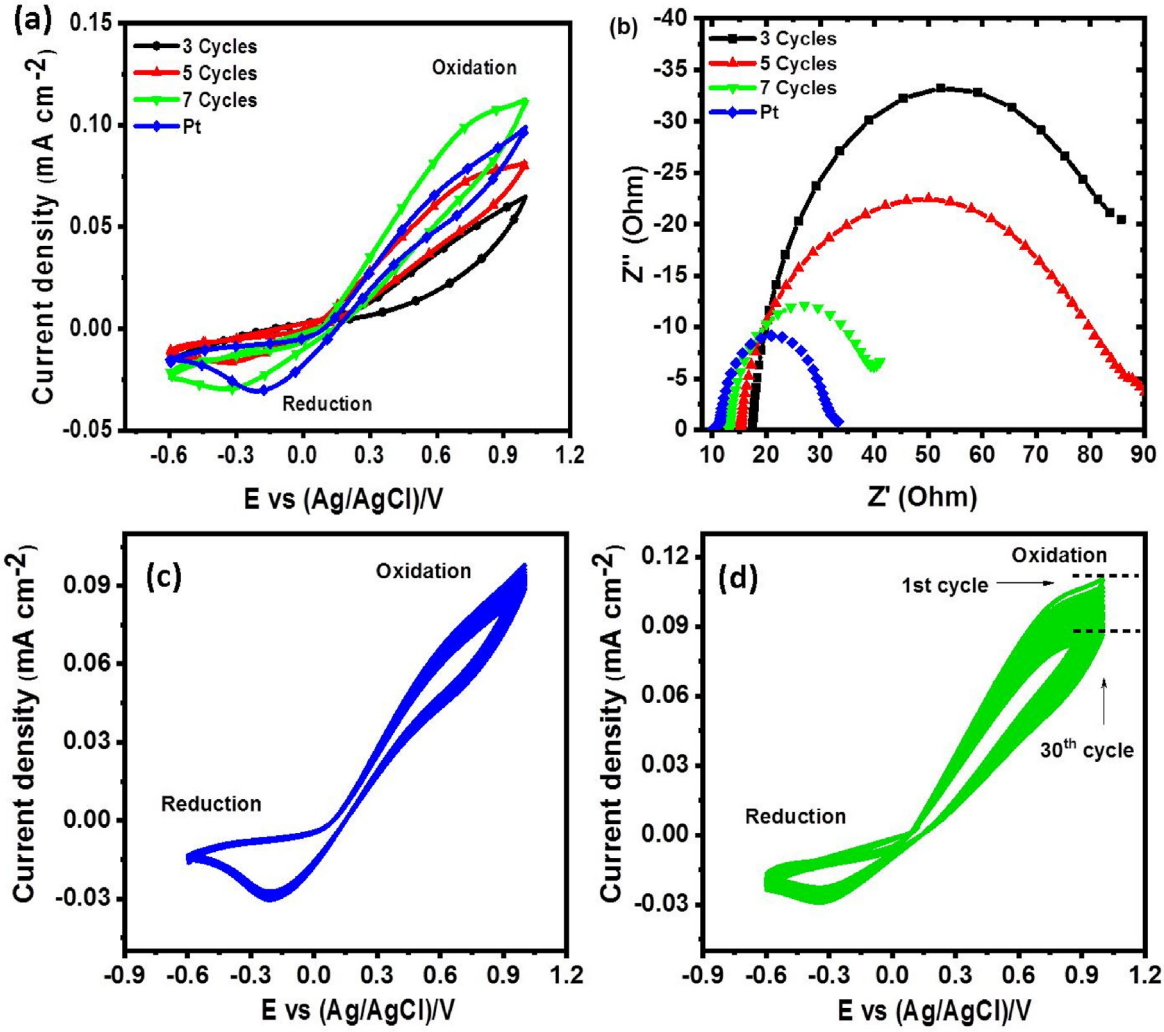

Fig. 6. (a–b) Cyclic voltammogram and Nyquist spectra of different CZTSSe CEs and Pt, respectively. (c) 30 consecutive cyclic voltammogram scanning for Pt CE and (d) 30 consecutive cyclic voltammogram scanning for the best performing CZTSSe CE (7 cycles).

Nyquist plots for the symmetrical cells fabricated with different electrodes. The size of the semicircle is assigned to the charge transfer resistance (R_{ct}) that is the most important characteristic to demonstrate the electron transfer of different CEs for electrolyte reduction [45,46]. A lower R_{ct} increases the rate of electron transfer at the CE/electrolyte interface for catalytic reduction of electrolyte and consequently results in less recombination [21,45,46]. Table 2 shows the obtained R_{ct} values for the fabricated devices. The simulated R_{ct} value for CZTSSe CE after 7 cycles of spin coating, a bit higher than for the Pt CE, confirming CZTSSe CE can exhibit excellent electrocatalytic activity for electrolyte reduction which is comparable to the standard Pt CEs. The series resistance (R_s) is defined by the intercept of the Nyquist plots (left side) with the horizontal axis which is very close for the CZTSSe and Pt CEs, see Table 2.

Table 2
Comparison of R_s (Ω) and R_{ct} (Ω) calculated from EIS measurements of symmetric cell configuration of spin-coated CZTSSe and Platinum CEs.

Types of CEs	3 Cycles	5 Cycles	7 Cycles	Pt
R_s (Ω)	17.2	15.4	13.19	10.1
R_{ct} (Ω)	95	67	49	25

Aside from high catalytic activity, chemical stability in the electrolyte containing triiodide/iodide redox couple is another major concern in the development of Pt-free CEs that affecting the potential applications of DSSCs. To evaluate the chemical stability of CEs in the iodine-based electrolyte, CE usually subjected to sequential CV scanning [10,23]. As shown in Fig. 6(c–d), the best performing CZTSSe CE (7 cycles) shows slow reduction in the oxidation (~20%) and the reduction current density peaks (~18%) after 30 cycles of CV which is comparable to that obtained using "standard" Pt CEs by (~12%) for oxidation (~11%) for reduction current density. Moreover, the E_{pp} undergo nearly no change for CZTSSe CE after multi-cycle successive CV scanning. This result demonstrates that CZTSSe CE materials are relatively stable and have properties that are comparable to those of Pt CE.

An important aspect of solar cell research and development is batch-to-batch reproducibility without large scale variations of the PV parameters. To assess the reproducibility of the counter electrode fabrication procedure, six different batches of DSSCs based on the CZTSSe and Pt CEs produced and the corresponding functional performances comparatively evaluated. Fig. 7 reports the performance parameters for each cell batch. Similar parameters for cells within the different batches can be observed. This similarity confirms the remarkable reproducibility of our solar cells within the

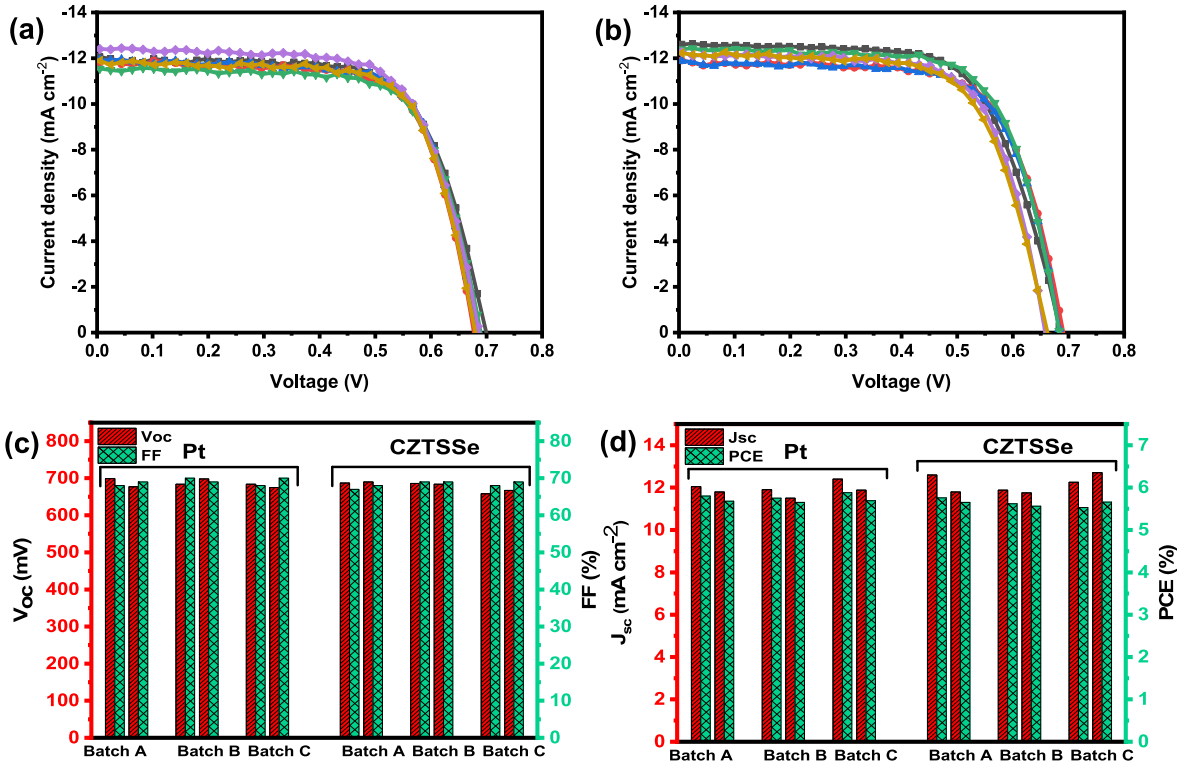

Fig. 7. Comparison between working parameters of different devices produced based on the Pt and CZTSSe CEs, highlighting the high reproducibility. (a and b) Current density-voltage curves of solar cells assembled with Pt and CZTSSe CEs respectively, under AM1.5G irradiation (100 mW cm^{-2}), (c) V_{oc} and FF, (d) J_{sc} and PCE.

different batches. In consideration of the similar PV parameters for all devices, CZTSSe CEs are effective for the fabrication of high-performance DSSCs with high reproducibility.

Similar to Pt materials, the transparent conducting oxide (TCO) glass substrate is also known as a high-cost component for DSSC [18–20]. Therefore, the design of a low-cost alternative TCO free substrate-based efficient CEs is of practical significance. Thus, we conducted more experiments to evaluate the application of CZTSSe/CP as a TCO and Pt free CE for DSSC. The electrocatalytic activity of as-synthesized CZTSSe nanosheets deposited on a CP was

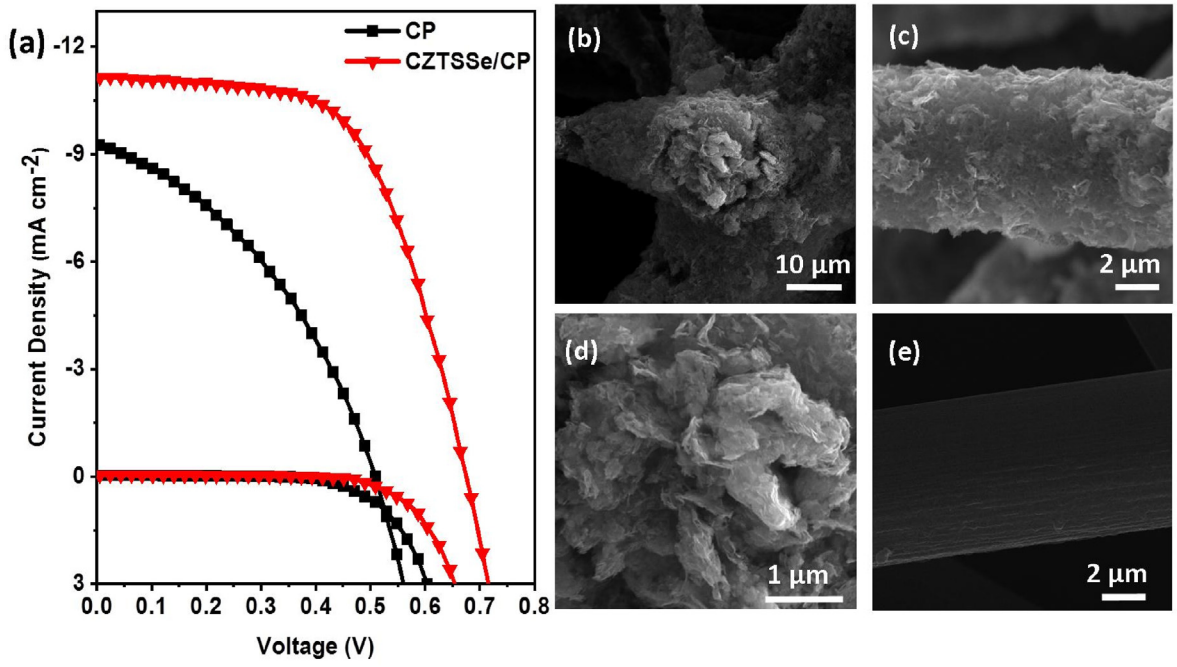

Fig. 8. (a) Current density-voltage curves of solar cells assembled with bare CP and CZTSSe/CP CEs, under AM1.5G irradiation (100 mW cm^{-2}) and dark conditions, (b–d) SEM images of CZTSSe deposited on CP at different magnifications and (e) SEM images of bare CP.

Table 3
Performance parameters of DSSCs fabricated using different CEs.

Sample	PCE/%	FF/%	V_{oc}/V	J_{sc}/mA cm^{-2}
Bare CP	1.76	38	0.50	9.27
CZTSSe/CP	4.60	63	0.67	10.9

investigated by fabrication of a series of DSSCs based on the bare CP and CZTSSe/CP CEs. Fig. 8 (a) displays the J-V curves obtained under one sun simulated sunlight at AM 1.5G (100 mW cm^{-2}) of DSSCs with different CEs. The calculated PV parameters of the corresponding devices are summarized in Table 3. The results show that the bare CP has poor catalytic activity. However, the CZTSSe/CP CEs resulted in an excellent PV performance. The device with bare CP CE exhibits PCE (1.76%) and CZTSSe/CP based DSSCs shows (4.60%). This may be mainly ascribed to the high surface area and excellent catalytic activity of homogenously deposited CZTSSe nanosheets on the surface of the fiber, which is confirmed by FESEM of CZTSSe/CP CE at different magnification (Fig. 8 (b)–(d)). For the comparison, Fig. 8 (e) displays FESEM of bare CP based CE.

4. Conclusions and perspectives

In conclusion, we have demonstrated a fast and highly reproducible solution-processable approach to synthesize CZTSSe with nanosheet morphology. Microstructure evaluation confirmed that the synthesized CZTSSe has nanosheet morphology with uniform distribution on the surface of the coating. EDS, Raman, XRD and XPS measurements verified the structure and composition of the CZTSSe nanosheets. The synthesized CZTSSe nanosheets exhibit good catalytic performance toward the reduction of the electrolyte and exhibited an impressive PCE of 5.73%, which is comparable to that obtained using “standard” Pt CEs (5.78%). The electrochemical measurements showed that the CE based on the CZTSSe nanosheets has strong catalysis ability and comparable R_{ct} and R_s with Pt. Multi-cycle successive CV scanning confirms that the as-prepared CZTSSe CE with high reproducibility exhibits good chemical stability in the electrolyte containing triiodide/iodide redox couple. The DSSCs assembled with CZTSSe/CP CEs as a FTO-Pt free device yield a PCE of 4.60%. These results provide a simple wet-chemistry synthesis of CZTSSe nanosheets and a viable spin-coating fabrication of CE as a prospective candidate to replace highly expensive Pt CEs.

5. Credit author statement

M.M.: Design the counter electrode, fabrication and characterization of solar cells, data analysis and draft the manuscript. M. L.: synthesis of CZTSSe nanosheets. G. S. S.: Conception, design and supervised the fabrication and characterization of photovoltaic devices and revised the manuscript. F.N.P: perform CV measurements. H.Z., Z.M.W., C.Y.L. and B. S.: revised the manuscript. D.R.R.: Design and supervised the synthesis and characterization of CZTSSe nanosheets. F. R: supervised and revised the manuscript. All authors contributed to revisions that brought it to its final form.

Declaration of competing interest

The authors declare that they have no known competing financial interests or personal relationships that could have appeared to influence the work reported in this paper.

Acknowledgements

We acknowledge funding from the Canada Foundation for Innovation for equipment and related operating funds and the Natural Science and Engineering Research Council (NSERC) of Canada for a Collaborative Research and Development project in partnership with MPB Technologies Inc. and Plasmionique Inc. F.R. is also supported by an NSERC Discovery Grant and is grateful to the Canada Research Chairs program for funding and partial salary support. M. M. is thankful to Fonds de recherche du Québec -Nature et technologies (FRQNT) for a PhD Scholarship (B2X). G. S. Selopal acknowledges the UNESCO Chair in MATECSS for a PDF Excellence Scholarship and funding from the University of Electronic Science and Technology of China. This work was supported in part by the National Science Foundation, Award# 1535876. D. R. Radu acknowledges NASA, Award # 80NSSC19M0201, supporting M.L. postdoctoral fellowship and the materials synthesis work.

Appendix A. Supplementary data

Supplementary data to this article can be found online at https://doi.org/10.1016/j.electacta.2020.135954.

References

[1] L. Suganthi, A.A. Samuel, Energy models for demand forecasting-A review, Renew. Sustain. Energy Rev. 16 (2012) 1223–1240, https://doi.org/10.1016/j.rser.2011.08.014.
[2] M.Z. Iqbal, S. Khan, Progress in the performance of dye sensitized solar cells by incorporating cost effective counter electrodes, Sol. Energy 160 (2018) 130–152, https://doi.org/10.1016/j.solener.2017.11.060.
[3] J. Wu, Z. Lan, J. Lin, M. Huang, Y. Huang, L. Fan, G. Luo, Y. Lin, Y. Xie, Y. Wei, Counter electrodes in dye-sensitized solar cells, Chem. Soc. Rev. 46 (2017) 5975–6023, https://doi.org/10.1039/c6cs00752j.
[4] B. O'Regan, M. Grätzel, A low-cost, high-efficiency solar cell based on dye-sensitized colloidal TiO_2 films, Nature 353 (1991) 737–740.
[5] S. Tai, C. Liu, S. Chou, F.S. Chien, J. Lin, T.W. Lin, Few-layer MoS_2 nanosheets coated onto multi-walled carbon nanotubes as a low-cost and highly electrocatalytic counter electrode for dye-sensitized solar cells, J. Mater. Chem. 22 (2012) 24753–24759, https://doi.org/10.1039/c2jm35447k.
[6] Q. Tang, J. Duan, Y. Duan, B. He, L. Yu, Recent advances in alloy counter electrodes for dye-sensitized solar cells. A critical review, Electrochim. Acta 178 (2015) 886–899, https://doi.org/10.1016/j.electacta.2015.08.072.
[7] M. Mohammadnezhad, G.S. Selopal, Z. Wang, B. Stansfield, H. Zhao, F. Rosei, Towards long-term thermal stability of dye-sensitized solar cells using multiwalled carbon nanotubes, Chempluschem 83 (2018) 682–690, https://doi.org/10.1002/cplu.201800046.
[8] M. Mohammadnezhad, G.S. Selopal, Z.M. Wang, B. Stansfield, H. Zhao, F. Rosei, Role of carbon nanotubes to enhance the long-term stability of dye-sensitized solar cells, ACS Photonics (2020), https://doi.org/10.1021/acsphotonics.9b01431.
[9] K.T. Dembele, G.S. Selopal, C. Soldano, R. Nechache, J.C. Rimada, I. Concina, S. Giorgio, F. Rosei, A. Vomiero, Hybrid carbon nanotubes-TiO_2 photoanodes for high efficiency dye-sensitized solar cells, J. Phys. Chem. C 117 (2013) 14510–14517.
[10] S. Yun, P.D. Lund, A. Hinsch, Stability assessment of alternative platinum free counter electrodes for dye-sensitized solar cells, Energy Environ. Sci. 8 (2015) 3495–3514, https://doi.org/10.1039/c5ee02446c.
[11] Z. Tong, S. Liu, X. Li, J. Zhao, Y. Li, Self-supported one-dimensional materials for enhanced electrochromism, Nanoscale Horizons 3 (2018) 261–292, https://doi.org/10.1039/c8nh00016f.
[12] S.K. Matta, K. Kakiage, S. Makuta, A. Veamatahau, Y. Aoyama, T. Yano, M. Hanaya, Y. Tachibana, Dye-anchoring functional groups on the performance of dye-sensitized solar cells: comparison between alkoxysilyl and carboxyl groups, J. Phys. Chem. C 118 (2014) 28425–28434, https://doi.org/10.1021/jp5088338.
[13] T. Daeneke, A.J. Mozer, Y. Uemura, S. Makuta, M. Fekete, Y. Tachibana, N. Koumura, U. Bach, L. Spiccia, Dye regeneration kinetics in dye-sensitized solar cells, J. Am. Chem. Soc. 134 (2012) 16925–16928, https://doi.org/10.1021/ja3054578.
[14] S. Yun, Y. Liu, T. Zhang, S. Ahmad, Recent advances in alternative counter electrode materials for Co-mediated dye-sensitized solar cells, Nanoscale 7 (2015) 11877–11893, https://doi.org/10.1039/c5nr02433a.
[15] K.S. Lee, K. Lee, H. Wang, N. Park, Y. Lee, O.O. Park, J. Hyeok, Dye-sensitized solar cells with Pt-and TCO-free counter electrodes, Chem. Commun. 46 (2010) 4505–4507, https://doi.org/10.1039/c0cc00432d.
[16] G.S. Selopal, R. Chahine, M. Mohammadnezhad, F. Navarro-Pardo, D. Benetti,

H. Zhao, Z.M. Wang, F. Rosei, Highly efficient and stable spray assisted nanostructured Cu_2S/Carbon paper counter electrode for quantum dots sensitized solar cells, J. Power Sources 436 (2019), 226849, https://doi.org/10.1016/j.jpowsour.2019.226849.

[17] X. Xin, M. He, W. Han, J. Jung, Z. Lin, Low-cost copper zinc tin sulfide counter electrodes for high-efficiency dye-sensitized solar cells, Angew. Chemie-Int. 50 (2011) 11739–11742, https://doi.org/10.1002/anie.201104786.

[18] G. Yue, J. Lin, S. Tai, Y. Xiao, J. Wu, A catalytic composite film of MoS_2/graphene flake as a counter electrode for Pt-free dye-sensitized solar cells, Electrochim. Acta 85 (2012) 162–168, https://doi.org/10.1016/j.electacta.2012.08.040.

[19] H. Kim, G. Veerappan, J.H. Park, Conducting polymer coated non-woven graphite fiber film for dye-sensitized solar cells: superior Pt-and FTO-free counter electrodes, Electrochim. Acta 137 (2014) 164–168, https://doi.org/10.1016/j.electacta.2014.06.012.

[20] Z. Xu, T. Li, Q. Liu, F. Zhang, X. Hong, S. Xie, C. Lin, X. Liu, W. Guo, Controllable and large-scale fabrication of rectangular CuS network films for indium tin oxide-and Pt-free flexible dye-sensitized solar cells, Sol. Energy Mater. Sol. Cells 179 (2018) 297–304, https://doi.org/10.1016/j.solmat.2017.12.024.

[21] H. Chen, D. Kou, Z. Chang, W. Zhou, Z. Zhou, S. Wu, Effect of crystallization of $Cu_2ZnSnS_xSe_{4-x}$ counter electrode on the performance for efficient dye-sensitized solar cells, ACS Appl. Mater. Interfaces 6 (2014) 20664–20669, https://doi.org/10.1021/am503963b.

[22] S.A. Patil, N. Mengal, A. Ali, S. Hoon, H. Kim, CuS thin film grown using the one pot, solution-process method for dye-sensitized solar cell applications, J. Alloys Compd. 708 (2017) 568–574, https://doi.org/10.1016/j.jallcom.2017.03.026.

[23] S. Yun, A. Hagfeldt, T. Ma, Pt-free counter electrode for dye-sensitized solar cells with high efficiency, Adv. Mater. 26 (2014) 6210–6237, https://doi.org/10.1002/adma.201402056.

[24] C. Wang, S. Yun, Q. Fan, Z. Wang, Y. Zhang, F. Han, Y. Si, A. Hagfeldt, A hybrid niobium-based oxide with bio-based porous carbon as an efficient electrocatalyst in photovoltaics: a general strategy for understanding the catalytic mechanism, J. Mater. Chem. A 7 (2019) 14864–14875, https://doi.org/10.1039/C9TA03540K.

[25] S. Yun, J.N. Freitas, A.F. Nogueira, Y. Wang, S. Ahmad, Z.S. Wang, Dye-sensitized solar cells employing polymers, Prog. Polym. Sci. 59 (2016) 1–40, https://doi.org/10.1016/j.progpolymsci.2015.10.004, doi.

[26] X. Miao, K. Pan, G. Wang, Y. Liao, L. Wang, W. Zhou, Well-dispersed CoS nanoparticles on a functionalized graphene nanosheet Surface : a counter electrode of dye-sensitized solar cells, Chem. Eur J. 20 (2014) 474–482, https://doi.org/10.1002/chem.201303558.

[27] J. Shen, D. Zhang, J. Li, X. Li, Z. Sun, S. Huang, Fabrication and evaluation of low-cost $Cu_2ZnSn(S,Se)_4$ counter electrodes for dye-sensitized solar cells, Nano-Micro Lett. 5 (2014) 281–288, https://doi.org/10.1007/bf03353759.

[28] X. Wang, Y. Xie, B. Bateer, K. Pan, Y. Jiao, N. Xiong, S. Wang, H. Fu, Selenization of Cu_2ZnSnS_4 enhanced the performance of dye-sensitized solar cells: improved zinc-site catalytic activity for I_3^-, ACS Appl. Mater. Interfaces 9 (2017) 37662–37670, https://doi.org/10.1021/acsami.7b09642.

[29] S.Y. Kim, T.R. Rana, J.H. Kim, D.H. Son, K.J. Yang, J.K. Kang, D.H. Kim, Limiting effects of conduction band offset and defect states on high efficiency CZTSSe solar cell, Nanomater. Energy 45 (2018) 75–83, https://doi.org/10.1016/j.nanoen.2017.12.031.

[30] Y. Gao, J. Wang, S. Mo, F. Wang, F. Long, Z. Zou, Synthesis of high-quality wurtzite Cu 2 $ZnSn(S_{1-x},Se_x)_4$ nanocrystals with non-toxic selenium precursor and the photoelectrochemical performance of ZnO NAs/CZTSSe heterojunction, Sol. RRL 2 (2018), 1800015, https://doi.org/10.1002/solr.201800015.

[31] M. Grossberg, J. Krustok, J. Raudoja, K. Timmo, M. Altosaar, T. Raadik, Photoluminescence and Raman study of $Cu_2ZnSn(Se_xS_{1-X})_4$ monograins for photovoltaic applications, Thin Solid Films 519 (2011) 7403–7406, https://doi.org/10.1016/j.tsf.2010.12.099.

[32] X. Zhou, N. Zhou, C. Li, H. Song, Q. Zhang, X. Hu, L. Gan, H. Li, J. Lü, J. Luo, J. Xiong, T. Zhai, Vertical heterostructures based on $SnSe_2/MoS_2$ for high performance photodetectors, 2D Mater. 4 (2017) 25048, https://doi.org/10.1088/2053-1583/aa6422.

[33] G. Marcano, C. Rincón, S.A. López, G. Sánchez Pérez, J.L. Herrera-Pérez, J.G. Mendoza-Alvarez, P. Rodríguez, Raman spectrum of monoclinic semiconductor Cu_2SnSe_3, Solid State Commun. 151 (2011) 84–86, https://doi.org/10.1016/J.SSC, 2010.10.015.

[34] R. Sun, D. Zhuang, M. Zhao, Q. Gong, M. Scarpulla, Y. Wei, G. Ren, Y. Wu, Beyond 11% efficient $Cu_2ZnSn(Se,S)_4$ thin film solar cells by cadmium alloying, Sol. Energy Mater. Sol. Cells 174 (2018) 494–498, https://doi.org/10.1016/j.solmat.2017.09.043.

[35] M. Danilson, M. Altosaar, M. Kauk, A. Katerski, J. Krustok, J. Raudoja, XPS study of CZTSSe monograin powders, Thin Solid Films 519 (2011) 7407–7411, https://doi.org/10.1016/j.tsf.2010.12.165.

[36] S.L. Chen, J. Tao, H.J. Tao, Y.Z. Shen, T. Wang, L. Pan, High-performance and low-cost dye-sensitized solar cells based on kesterite Cu_2ZnSnS_4 nanoplate arrays on a flexible carbon cloth cathode, J. Power Sources 330 (2016) 28–36, https://doi.org/10.1016/j.jpowsour.2016.08.134.

[37] R. Ma, F. Yang, S. Li, X. Zhang, X. Li, S. Cheng, Z. Liu, Fabrication of $Cu_2ZnSn(S,Se)_4$ (CZTSSe) absorber films based on solid-phase synthesis and blade coating processes, Appl. Surf. Sci. 368 (2016) 8–15, https://doi.org/10.1016/j.apsusc.2016.01.242.

[38] H. Wang, S. Huang, S. Wang, Z. Hu, G. Ding, X. Qian, Z. Chen, Colloid synthesis of $CuFeSe_2$ nanocubes as efficient electrocatalysts for dye-sensitized solar cells, J. Electroanal. Chem. 834 (2019) 26–32, https://doi.org/10.1016/j.jelechem.2018.12.005.

[39] M. Mohammadnezhad, G.S. Selopal, N. Alsayyari, R. Akilimali, F. Navarro-pardo, Z.M. Wang, B. Stansfield, H. Zhao, F. Rosei, CuS/Graphene nanocomposite as a transparent conducting oxide and Pt-free counter electrode for dye-sensitized solar cells, J. Electrochem. Soc. 166 (2019) 3065–3073, https://doi.org/10.1149/2.0121905jes.

[40] F. Navarro-Pardo, D. Benetti, H. Zhao, V. Castano, A. Vomiero, F. Rosei, Platinum/Palladium hollow nanofibers as high-efficiency counter electrodes for enhanced charge transfer, J. Power Sources 335 (2016) 138–145, https://doi.org/10.1016/j.jpowsour.2016.10.011.

[41] S. Thomas, T.G. Deepak, G.S. Anjusree, T.A. Arun, S.V. Nair, A.S. Nair, A review on counter electrode materials in dye-sensitized solar cells, J. Mater. Chem. A 2 (2014) 4474–4490, https://doi.org/10.1039/c3ta13374e.

[42] E. Palomares, J.N. Clifford, S.A. Haque, T. Lutz, J.R. Durrant, Control of charge recombination dynamics in dye sensitized solar cells by the use of conformally deposited metal oxide blocking layers, J. Am. Chem. Soc. 125 (2003) 475–482, https://doi.org/10.1021/ja027945w.

[43] F. Navarro-Pardo, D. Benetti, J. Benavides, H.G. Zhao, S.G. Cloutier, V.M. Castano, A. Vomiero, F. Rosei, Nanofiber-structured TiO_2 nanocrystals as a scattering layer in dye-sensitized solar cells, ECS J. of Solid State Sci. Technol. 6 (2017) 32–37, https://doi.org/10.1149/2.0181704jss.

[44] A. Zaban, M. Greenshtein, J. Bisquert, Determination of the electron lifetime in nanocrystalline dye solar cells by open-circuit voltage decay measurements, ChemPhysChem 4 (2003) 859–864, https://doi.org/10.1002/cphc.200200615.

[45] M. Wu, X. Lin, Y. Wang, L. Wang, W. Guo, D. Qi, X. Peng, A. Hagfeldt, M. Grätzel, T. Ma, Economical Pt-free catalysts for counter electrodes of dye-sensitized solar cells, J. Am. Chem. Soc. 134 (2012) 3419–3428, https://doi.org/10.1021/ja209657v.

[46] J. He, L.T.L. Lee, S. Yang, Q. Li, X. Xiao, T. Chen, Printable highly catalytic Pt-and TCO-free counter electrode for dye-sensitized solar cells, ACS Appl. Mater. Interfaces 6 (2014) 2224–2229, https://doi.org/10.1021/am4057375.